HAL open science

Optimization of Instrumental Spectral Configurations for the Split-Window Method in the Context of the TRISHNA Mission

Thomas H.G. Vidal, Frédéric Jacob, Albert Olioso, Philippe Gamet

▶ **To cite this version:**

Thomas H.G. Vidal, Frédéric Jacob, Albert Olioso, Philippe Gamet. Optimization of Instrumental Spectral Configurations for the Split-Window Method in the Context of the TRISHNA Mission. IEEE Transactions on Geoscience and Remote Sensing, 2021, pp.1-14. 10.1109/TGRS.2021.3099967 . hal-03336205v2

HAL Id: hal-03336205

https://hal.science/hal-03336205v2

Submitted on 10 Jan 2022

HAL is a multi-disciplinary open access archive for the deposit and dissemination of scientific research documents, whether they are published or not. The documents may come from teaching and research institutions in France or abroad, or from public or private research centers.

L'archive ouverte pluridisciplinaire **HAL**, est destinée au dépôt et à la diffusion de documents scientifiques de niveau recherche, publiés ou non, émanant des établissements d'enseignement et de recherche français ou étrangers, des laboratoires publics ou privés.

Final version accepted for publication

Optimization of Instrumental Spectral Configurations for the Split Window Method in the Context of the TRISHNA Mission

Thomas H. G. Vidal, Frederic Jacob, *Senior Member, IEEE*, Albert Olioso and Philippe Gamet

***Abstract*—We propose an original approach to optimize the TRISHNA instrument spectral configuration for the Split-Window (SW) method. First, we consider as input of end-to-end simulations an emissivity dataset that accounts for cavity effect within vegetation canopy. Second, we propose a bi-dimensional approach where both locations of TRISHNA SW channels, namely λ_c^{TIR3} and λ_c^{TIR4}, can slide within predefined spectral intervals. We report a large sensitivity to channel positions, with variations of RMSE on retrieved land surface temperature up to 3 K. Our bi-dimensional approach shows that this sensitivity is consistent with the underlying assumptions of the SW method. Indeed, two regions are observed in the $(\lambda_c^{TIR3}, \lambda_c^{TIR4})$ space: (1) an unfavorable region corresponding to $\lambda_c^{TIR3} \leq 10.0$ μm, where large RMSE values are ascribed to large differences between emissivities in both SW channels, and (2) a favorable region corresponding to $\lambda_c^{TIR3} \geq 10.3$ μm, where differences between emissivities in both SW channels are small, and where RMSE values are driven by the differences between atmospheric transmittance in both SW channels. Overall, it is necessary to better account for the difference in surface emissivities between the two SW channels, whereas disregarding the cavity effect within vegetation canopy is not critical. Eventually, our bi-dimensional approach permits to define an optimal position for λ_c^{TIR3} at 10.6 μm, which induces a larger robustness to uncertainties on channel positions. By applying our study on two structurally different SW formulations and addressing impacts of uncertainties on land surface emissivity and atmospheric water vapor content, we show that these results can be generalized to other SW formulations.**

***Index Terms*—Thermal infrared remote sensing, Satellite mission design, Spectral channel positioning, Split Window method, Vegetation canopy - scaled cavity effect, Mercury - Cadmium - Telluride cooled detectors, Sensitivity analysis**

I. Introduction

SINCE the 1980's, remote sensing has become a primary mean for geosciences, notably because of its ability to retrieve land surface temperature (LST) from satellite observations on a global scale. Indeed, knowledge of LST is useful for the monitoring and modeling of related geophysical processes, including radiation budgets [1]–[5], soil water depletion through evapotranspiration [6]–[17], or photosynthesis and soil respiration [18]–[20]. The efficient characterization of these processes is paramount for agricultural and water resources management [21], especially in a global warming context, which makes equally important the efficient retrieval of LST. Such need for remote sensing of LST has translated in a recent soar of related satellite missions, including the launch of the NASA ECOsystem Spaceborne Thermal Radiometer Experiment on Space Station (ECOSTRESS) in 2018 [22], [23], the ESA future High Spatio-Temporal Resolution Land Surface Temperature Mission (HSTR LSTM, [24]), and the French (CNES) / Indian (ISRO) Thermal infraRed Imaging Satellite for High-resolution Natural resource Assessment (TRISHNA) mission [25].

An overview of the TRISHNA mission can be found in [26]. The TRISHNA satellite will embark both a visible / shortwave infrared sensor and a thermal infrared (TIR) one. The mission addresses 6 major themes from scientific research to development of applications: (1) terrestrial ecosystem stress and water use, (2) coastal and inland hydrological processes, (3) urban environment (e.g. urban heat island), (4) geological phenomena (e.g., geothermal exploration), (5) cryospheric processes (e.g., snow melt runoff), and (6) atmospheric characterization. Among these objectives, the first two are the design drivers of the mission and are of critical interest in a climate change context, notably for inter-tropical regions in India, for sub-humid regions in southern France, or for semi-arid to arid regions in the Mediterranean basin. In order to efficiently serve these objectives, including for instance high resolution monitoring of both water stress at crop field scale and heat islands in urban areas, the TRISHNA mission involves several key features. First, the platform is set to an approximately 760 km sun-synchronous orbit, which allows a $\sim$60 m spatial resolution and a three-day revisit rate with a global coverage, and an average local overpass time of 1 p.m. LTDN (Local Time at Descending Node). Second, the baseline TIR spectral configuration includes four channels centered at 8.6, 9.1, 10.4 and 11.6 μm, in accordance with previous studies on the TRISHNA precursor MISTIGRI mission [26], [27]. This permits to characterize the spectral variability depicted by land surfaces, as well as to retrieve land surface temperature. Third, the four TIR channels rely on second generation Mercury - Cadmium - Telluride (MCT) cooled detectors, providing a much better signal-to-noise ratio

Manuscript received MMMM DD, YYYY; revised MMMM DD, YYYY and MMMM DD, YYYY; accepted MMMM DD, YYYY. Date of publication MMMM DD, YYYY; date of current version MMMM DD, YYYY. This work was funded by the French Space Agency (CNES, contract 181154) in the context of the preparation of the TRISHNA mission.

Thomas H. G. Vidal is with ACRI-ST, Toulouse, France (e-mail: thomas.vidal@acri-st.fr). Frédéric Jacob is with UMR LISAH, University of Montpellier, IRD, INRAE, Institut Agro - Montpellier SupAgro, Montpellier, France (e-mail: frederic.jacob@ird.fr). Albert Olioso is with INRAE, UMR 1114 EMMAH, France (e-mail: albert.olioso@inrae.fr). Philippe Gamet is with CNES (French Space Agency) and Centre d'Etudes Spatiales de la BIOsphere CESBIO, Université de Toulouse, Toulouse, France(e-mail: philippe.gamet@cnes.fr).

as compared to microbolometer based detectors. And fourth, the acquisition principle, based on a rotating scanning mirror, allows frequent calibration of the signal on deep space and on an onboard black body, as well as wider swath leading to shorter revisit.

Among the existing methods for LST retrieval (see [28]–[30] for reviews on the matter), two were selected for application during the TRISHNA mission, namely the Temperature-Emissivity Separation (TES) method and the Split Window (SW) method. The TES method was chosen as a primary method since it allows a direct estimation of land surface radiometric temperature from a unique snapshot of multispectral imagery without any ancillary information on the observed scene, which strengthens the capability of the TRISHNA mission to monitor land surface temperature with a three day revisit rate. TES was also selected for maturity, since its performance has been continually evaluated and optimized by numerous studies over the last 20 years, including its use for producing NASA LST products from the MODerate resolution Imaging Spectroradiometer (MODIS), the Visible Infrared Imaging Radiometer Suite (VIIRS), and the ECOSTRESS sensors [31]–[43]. Consequently to the location of two channels within the [9.5-12.5] μm spectral range, the SW method was selected as a secondary method for several reasons. First, the SW method can be used on areas where the TES method underperforms, namely grey-body like targets such as water, ice, snow or dense vegetation, for which emissivity is known and SW method performs correctly [30]. Second, using the SW method as a backup solution strengthens the TRISHNA mission capability in case of channel failure over the [8-9.5] μm spectral range, since it makes use of two channels only over the [9.5-12.5] μm spectral range. Third, the SW method is applied directly on measured brightness temperature without any prior atmospheric corrections. Fourth, the visible / shortwave infrared instrument onboard the TRISHNA platform allows the simultaneous collection of ancillary information for the SW method, including observations for potentially retrieving waveband emissivity on the basis of fractional vegetation cover and / or NDVI [44]–[50], as well as characterization of atmospheric transmittance for the derivation of atmospheric water vapor content (AWVC) [51]–[53].

Many SW formulations have been proposed over the last three decades (see [30] for a review), all of them assuming a priori knowledge about target emissivity. They are either linear [48], [54], [55], non-linear [56], [57], dependent upon AWVC [51], [58], or dependent upon view zenith angle [49], [59]. Each SW formulation has to be calibrated over a dataset of both measured brightness temperatures and target radiometric temperature, with possibly additional inclusion of AWVC and land surface emissivity (LSE). Previous studies usually relied on measured and/or simulated datasets, where measured datasets include laboratory and field-based data. Overall, previous works are questionable on two issues, amongst others. The first issue is related to the calibration datasets that involve emissivity spectra from single or linearly mixed laboratory samples. Consequently, they are not representative of actual land surface conditions, especially for vegetation covers with cavity effect (i.e., emissivity increase) due to in-canopy radiation trapping [50], [60]–[68]. The second issue is related to the method used for designing the optimal spectral configuration. Indeed, most studies compared SW performance for several predefined spectral configurations, whereas a more appropriate way consists of identifying an optimal pair (i.e., minimum errors on LST retrieval) within the spectral space defined by the sliding of the two SW channels [42], [69].

The current study aims to find the optimal positions of the TRISHNA SW channels, by analyzing the retrieval performance of a selected SW method over a simulated dataset. First, a bi-dimensional approach is used, where the positions of both SW channels can slide within the [9.5-12.5] μm interval, with possible overlays. This bi-dimensional approach permits to easily identify extreme values for the performance indicators of the SW method, within the space defined by the positions of the two channels. Besides, it also permits to find the spectral configuration that is the most robust to uncertainties on channel positions due to instrumental design. Second, the simulated dataset to be used for analyzing the retrieval performance of the SW method includes the emissivity spectra dataset proposed by [38]. This dataset provides more realistic and representative emissivity spectra to be used in TIR studies, since it accounts for cavity effect due to in-canopy radiance trapping. In order to make our results more generic, we compare the sensitivity results obtained with the selected SW formulation to those obtained with a structurally very different one.

We first present the SW method chosen for this study in Section II. Afterwards, Section III presents an overview of the end-to-end simulator used to generate the calibration / validation dataset for the SW method, along with its implementation for the TRISHNA study. The setup of the sensitivity analysis is presented in Section IV, and subsequent results in Section V. We discuss these results and conclude in Sections VI and VII, respectively.

II. The Split-Window method

The SW approach was originally developed by [54] on the basis of a differential analysis of the radiative transfer equation over several channels. It has been implemented for most existing TIR sensors and permits to derive surface radiometric temperature from measurements in two TIR channels within the [9.5 - 12.5] μm spectral interval [42], [70]. The SW method is based on the hypothesis that most natural surfaces depict flat emissivity spectra within this TIR interval, which implies that the difference in brightness temperatures measured in the two adjacent channels is only due to the difference in atmospheric perturbations between the two channels (i.e., absorption and emission). Therefore, the atmospheric effects can be directly corrected by formulating the target radiometric temperature T_{sur}^{SW} as a function of the two measured brightness temperatures. Besides, considering a spectral interval where land surface emissivity in both SW channels is nearly equal, the method should performs well if using a spectral channel with significant atmospheric perturbations and another one with low atmospheric perturbations.

Several SW formulations using more than two channels have been proposed, notably a three-channels version for

sea surface temperature measurements that makes use of a third mid-infrared channel corresponding to low atmospheric absorption [70], [71], and a four-channels version for land surface temperature measurements that makes use of two more TIR channels within the [7.5 - 9.5] μm spectral interval [72]. We disregard the three-channels SW formulation, since the TRISHNA instrument does not include a mid-infrared channel. Although applicable with the TRISHNA configuration, we also disregard the four-channels SW formulation. Indeed, the SW method is a backup method for the TRISHNA mission, and the position of the two TRISHNA channels within the [7.5 - 9.5] μm spectral interval are primarily constrained by the TES method. Overall, we favor the use of a two-channels SW method because it is a mature method that has been extensively studied and applied for previous TIR satellite missions. Further, we consider two-channels within the [9.5-12.5] μm spectral range, since using one or two channels in the [8-9.5] μm spectral range induces large errors on temperature retrievals [42].

For the TRISHNA instrument, we select the non-linear SW formulation proposed by [51]. Motivations for this choice are the following. First, it is a quadratic SW formulation, which has been proved to be more efficient for LST retrieval than linear methods [30], [69], since the latter introduce larger errors through the linearization of the radiative transfer equation. Second, it is a physically-based and AWVC-dependent formulation that has been extensively investigated (e.g., [42], [51], [73], [74]). Indeed, SW formulations that do not account for AWVC perform well for dry atmospheres only (i.e., AWVC < 2.5 g.cm^{-2}, [30]). Therefore, an AWVC-dependent SW formulation is necessary for the TRISHNA mission that addresses tropical and equatorial regions with large AWVC (> 2.5 g.cm^{-2}). Moreover, measurements of the AWVC are likely to be available on the TRISHNA platform thanks to a water vapor channel at 0.910 μm [75], [76].

The SW formulation proposed by [51] was shown to retrieve surface temperatures within a 1.3 K error margin, even in wet atmospheric conditions. It is formulated as followed:

$$\begin{aligned} T_{sur}^{SW} = T_{bx} + a_0 + a_1(T_{bx} - T_{by}) + a_2(T_{bx} - T_{by})^2 \\ +(b_0 + c_0.\text{AWVC})(1 - \langle\epsilon\rangle_{x,y}) \\ +(b_1 + c_1.\text{AWVC})\Delta_{x,y}\epsilon \end{aligned} \quad (1)$$

where T_{bx} and T_{by} are the brightness temperatures measured in the two channels selected for the SW application such as $\lambda_x < \lambda_y$. $\langle\epsilon\rangle_{x,y}$ and $\Delta_{x,y}\epsilon$ are respectively emissivity mean value and difference between both channels. The SW coefficients a_0, a_1, a_2, b_0, b_1, c_0 and c_1 have to be calibrated over a representative database of measured brightness temperatures covering wide ranges of surface emissivities and atmospheric conditions. This SW formulation requires knowledge of land surface emissivities in both SW channels, notably in order to account for the difference in emissivity between both channels. Future TRISHNA studies should focus on the development of an optimal method to derive emissivity from visible data, by using relationships between emissivity and fractional vegetation cover or NDVI [47], [50]. Therefore, these emissivities may be obtained via onboard measurements from the TRISHNA visible sensor.

III. Simulating the calibration / validation dataset

Our method to find the optimal positions for the TRISHNA SW channels relies on analyzing the retrieval accuracy on surface radiometric temperature, for several pairs of SW channels within the [9.5-12.5] μm spectral interval. For this purpose, we use a simulated dataset of TRISHNA measurements, along with corresponding reference values for land surface emissivity (waveband values) and radiometric temperature. The calibration / validation dataset to be used is generated using the Python End-to-end Remote SEnsing intrUment Simulator (PERSEUS), developed specifically for the TRISHNA mission. In this section, we offer a brief description of PERSEUS, as well as its implementation in the context of the TRISHNA mission. A more detailed presentation of PERSEUS can be found in [77].

A. PERSEUS overview

PERSEUS was developed specifically for TRISHNA studies in order to respond to the need for a modular, versatile and fast computing simulator, notably because of the large number of simulations to be conducted for our sensitivity analysis. It permits to compute end-to-end simulations for a given operating TIR sensor by including the following modules.

1) The computation of Top Of Atmosphere (TOA) radiance spectrum over the TIR domain via the radiative transfer module, which entry parameters are the scene surface properties such as land surface emissivity spectrum and radiometric temperature, as well as the associated atmospheric profile. For this computation, the module relies on the COMANCHE radiative transfer tool [78] which is based on MODTRAN 5.2 [79].
2) An instrument module that simulates the signal modifications between the TOA radiances and the Out of Sensor (OS) radiances. These modifications include (1) the convolution of the input signal with the Instrumental Spectral Response Function (ISRF) and (2) the application of instrumental noise. Note that ISRF application can be conducted on any spectrum beyond the TOA radiances, including for instance surface emissivity or radiance spectra.
3) An inversion module that permits to retrieve, via the application of a SW method, land surface radiometric temperature from the measured OS radiance.

Figure 1 presents a schematic overview of PERSEUS and its three aforementioned modules. An extensive description of these modules can be found in [77].

B. PERSEUS implementation in the context of the TRISHNA mission

In order to compute a dataset of TOA radiances, we first make use of the emissivity dataset obtained by [38]. This dataset includes 271 emissivity spectra of vegetation

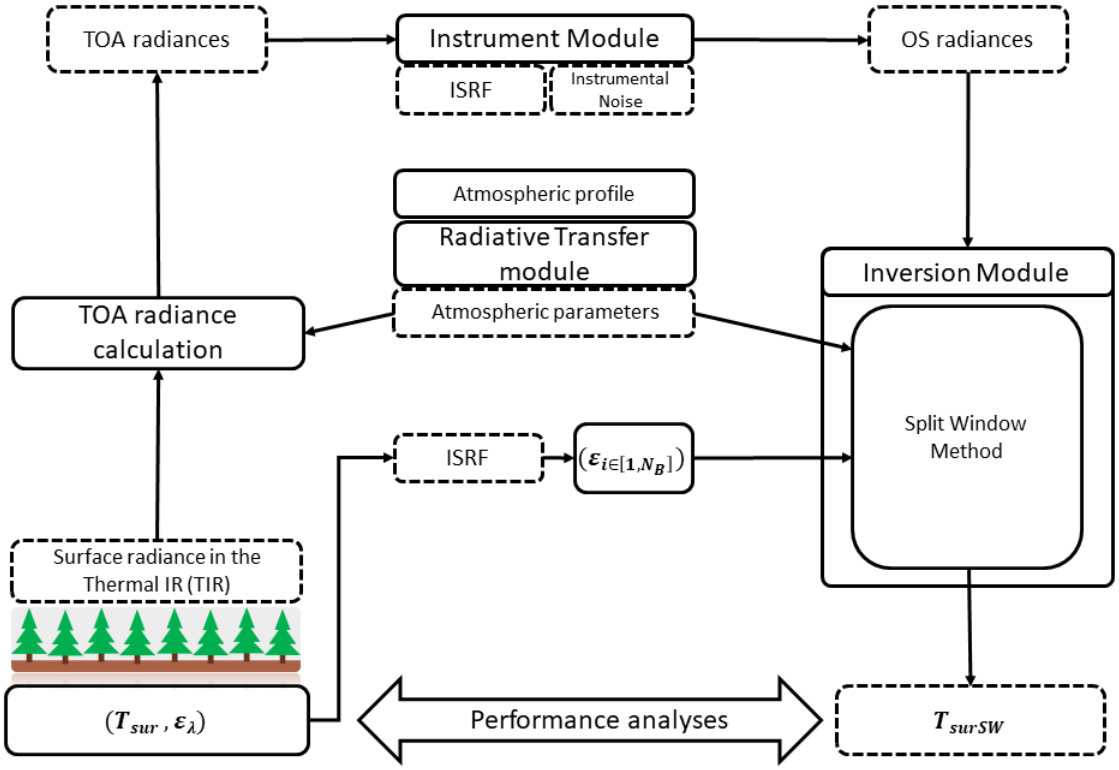

Fig. 1. Schematic overview of the PERSEUS tool that we use to generate a calibration/validation dataset for any SW method to be analysed. The three PERSEUS modules are: the radiative transfer module, the instrument module and the inversion module. The variables calculated by the simulator are highlighted in dotted lines.

TABLE I
SUMMARY OF THE SOIL AND VEGETATION PARAMETERS USED AS INPUT FOR THE OBTAINING OF THE 'SAIL271' DATASET (FROM [38]).

Parameters	Values
Number of soil reflectance spectra	313
Number of leave reflectance / transmittance spectra	64
LAI	0, 0.25, 0.5, 1, 2, 4, 7
ALA	15°, 35°, 55°, 75°
View zenith angle	Nadir

canopy over soils, simulated with the SAIL-Thermique model over a large range of Leaf Area Index (LAI), Average Leaf Angle (ALA), soils reflectance spectra, and leave transmittance/reflectance spectra (Table I), and statistically selected via the Spectral Angle Mapper algorithm (SAM, [80]) to avoid redundant spectra. The SAIL-Thermique model [50], [81] takes into account important three-dimensional physical phenomena, notably radiance trapping and resulting cavity effect with an increase of emissivity. All emissivity spectra were simulated by considering a nadir observation direction, because angular variation of canopy emissivity are low between nadir and 40° [50], [82], [83], and because the maximum view zenith angle for the TRISHNA sensor is 34°. The resulting dataset of emissivity spectra is hereafter called 'SAIL271', and represented in Figure 2.

We then associate each of the 'SAIL271' spectra with 24 atmospheric profiles selected from the TIGR database [84]. The selection of these 24 atmospheric profiles aims to reduce computation load while preserving the envelope of the original TIGR dataset in the (T_{eq}^{atm}, AWVC) space (Figure 3), where the equivalent atmospheric temperature T_{eq}^{atm} is the averaged temperature obtained by weighting atmospheric temperatures with atmospheric humidity [85]. Comparison between Figure 3(a) and (b) indicates that the density of the selected subset differs from the original dataset, the latter including more dry atmospheres (AWVC $<$ 2.5 g.cm^{-2}) than wet atmospheres (AWVC $\geq$ 2.5 g.cm^{-2}). Nonetheless, this new distribution permits to give weight to atmospheric conditions of humid climates, which are of uppermost interest for the TRISHNA mission. The selected subset of atmospheric profiles is hereafter labelled 'TIGR24'. It contains 13 wet atmospheres and 11 dry ones. The selection of the 'TIGR24' subset and the subsequent weight given to wet atmosphere conditions will be discussed in section VI.

Eventually, each possible combination of 'SAIL271' spectra and 'TIGR24' profiles is associated to five surface radiometric temperatures T_{sur} following the criteria $T_{sur} = [T_{skin} - 5\text{K}; T_{skin}; T_{skin} + 5\text{K}; T_{skin} + 10\text{K}; T_{skin} + 15\text{K}]$, where T_{skin} is the temperature at the lower level of the corresponding atmospheric profile. For a given spectral configuration with two SW channels, the $271 \times 24 \times 5 = 32\,520$ PERSEUS simulations are then carried out in order to calculate the TOA radiances at nadir for each possible combination of surface emissivity spectra, atmospheric profile and surface

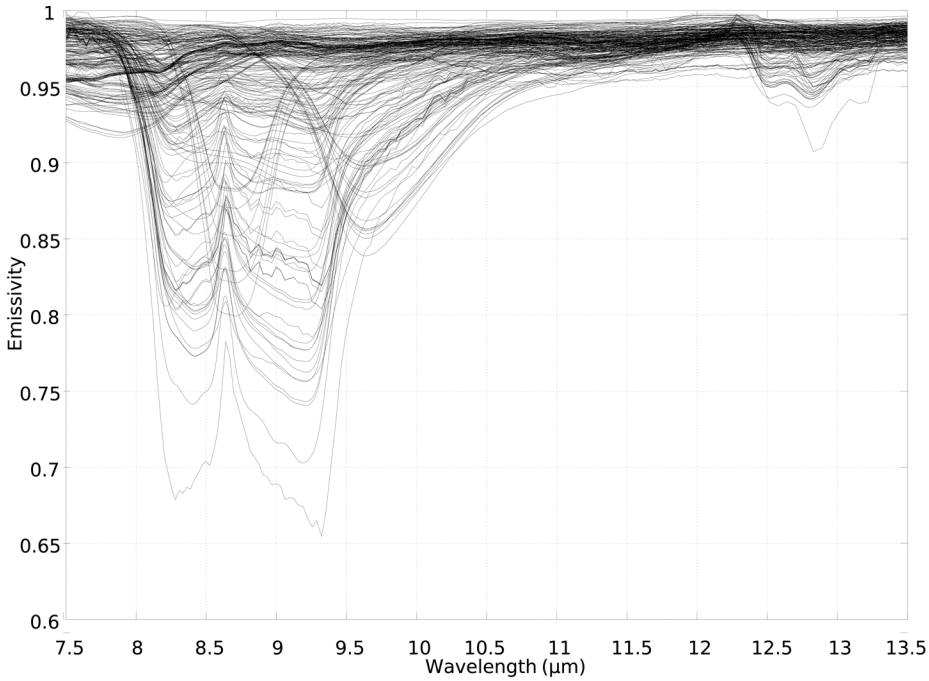

Fig. 2. The 271 emissivity spectra of the 'SAIL271' dataset, generated with the SAIL-Thermique model for a large panel of vegetation canopies over soils.

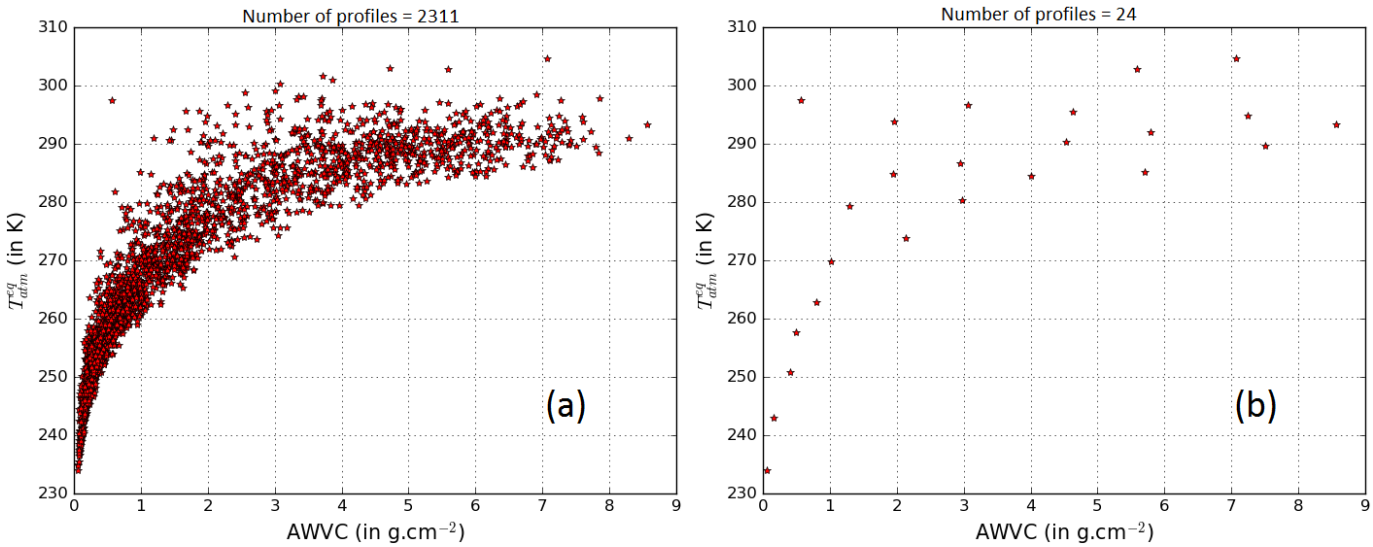

Fig. 3. Representation of the atmospheric profiles in the T_{eq}^{atm}/AWVC space for (a) the complete TIGR dataset, and (b) the 'TIGR24' subset.

radiometric temperature. This results in a dataset of TOA radiances which is likely to represent various surface and atmospheric conditions. A more extensive description of the obtaining of the TOA dataset can be found in [77].

IV. Setup for the Optimization of the Channels Wavelengths

A. ISRF variations

In order to constrain the spectral configuration of the TRISHNA TIR sensor, we analyze the sensitivity of the SW method defined in equation (1) to channel positions, *i.e.*, to their central wavelengths $(\lambda_c^i)_{i\in\{TIR3,TIR4\}}$. The ISRF of the reference TRISHNA TIR spectral configuration is composed of 4 TIR spectral channels labelled TIR1, TIR2, TIR3 and TIR4 with respective central wavelength at 8.6, 9.1, 10.4 and 11.6 μm.

We first define the spectral intervals of variation for λ_c^{TIR3} and λ_c^{TIR4}, namely [9.5 - 11] μm and [10.5 - 12] μm, respectively. These spectral intervals are chosen to account for constraints on instrumental design, as well as to assess the impact on the SW performance of both ozone absorption feature at 9.7 μm and SW channel proximity. Afterwards,

we consider simultaneous sliding of both channels in their respective spectral interval by steps of 0.1 μm, with a criterion on channels order that includes superimposition, *i.e.*, $\lambda_c^{TIR3} \leq \lambda_c^{TIR4}$. This two-dimensional approach permits to visualize local minima of error in the $(\lambda_c^{TIR3}, \lambda_c^{TIR4})$ space, and therefore to find an optimal spectral configuration for TIR3 and TIR4. The sliding process results in 241 ISRFs which permit to compute 241 $\times$ 32 520 = 7 837 320 OS radiances L^{OS}. The aforementioned setup is summarized in Table II.

B. Instrumental noise application

For the computation of each OS radiances L^{OS} thus obtained, we account for the corresponding TRISHNA instrumental noises, by using the following noise model for each channel i:

$$\text{Ne}\Delta L_i = \sqrt{a_i + b_i\, L_i} \tag{2}$$

where the term a_i accounts for both the dark current noise and the quantification noise, while the term $b_i\, L_i$ represents the shot noise, modelled by a Poisson process. Nominal values for both a_i and b_i parameters are given in Table II for both channels. Practically, the instrumental noise is applied on the TOA radiances after convolution with the ISRF, and implemented for each channel i as a white Gaussian noise with standard deviation equal to $\text{Ne}\Delta L_i$. The values in Table II are based on the preliminary data of $\text{Ne}\Delta L_i$ provided by the detector manufacturer, which satisfy the TRISHNA specification of a $\text{Ne}\Delta T < 0.25$ at 300K for TIR3 and TIR4 channels.

C. Criterion for the optimization of the channel wavelengths

Our criterion for the optimization of the channel wavelengths is the calibration RMSE of the SW formulation described in equation (1). This calibration is conducted for each aforementioned spectral configuration using its respective set of 32 520 OS radiances L^{OS}, as defined in section IV-A. The calibration RMSE is calculated via:

$$\text{RMSE}(T_{sur}^{SW}) = \sqrt{\frac{\sum_{N_s}(T_{sur} - T_{sur}^{SW})^2}{N_s}} \tag{3}$$

with T_{sur} the reference surface radiometric temperature (see section III-B and Figure 1), T_{sur}^{SW} the SW surface temperature retrieved with the calibrated SW coefficients, and N_s the number of OS radiances considered for each spectral configuration ($N_s = 32\,520$). This calculation of the calibration RMSE using our set of OS radiances permits to account for a large variability of input parameters, and therefore increases the robustness of our results.

It is not possible to use the common Leave One Out Cross Validation (LOOCV) procedure [86], because of constraints on computation load. In order to validate the calibration RMSE as a criterion for the optimization of the channel wavelengths, we conduct a calibration / validation protocol for each calculation of SW coefficients that correspond to a spectral configuration (i.e., a pair of $(\lambda_c^{TIR3}, \lambda_c^{TIR4})$). To that purpose, we first randomly split the set of 32 520 OS radiances L^{OS} obtained in two subsets of equal capacity, *i.e.*, 16 260 OS radiances

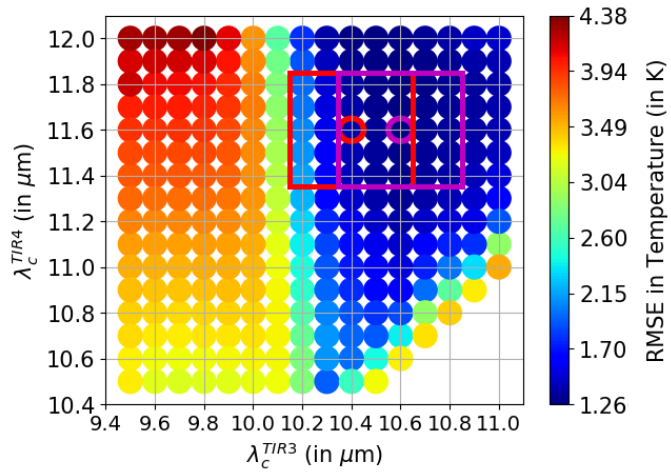

Fig. 4. RMSE values of the SW calibration for the 241 spectral configurations. The red and purple circles highlight the reference spectral configuration with $\text{RMSE}_{cal}(T_{sur}^{SW})$ = 1.39 K, and the optimized one with $\text{RMSE}_{cal}(T_{sur}^{SW})$ = 1.28 K, respectively. The red and purple rectangles highlight the robustness of the configurations to a 0.2 μm uncertainty on channel positions.

each. Afterwards, we (1) calibrate the SW coefficients over the first subset along with the corresponding calibration RMSE (equation 3), and (2) apply the calibrated SW method over the second subset and calculate the corresponding validation RMSE with equation 3.

This calibration / validation protocol introduces a supplementary variability in the RMSE variation across the $(\lambda_c^{TIR3}, \lambda_c^{TIR4})$ space, and therefore enhances the robustness of the results. As such, the obtained RMSE values for calibration and validation depict identical variations across the $(\lambda_c^{TIR3}, \lambda_c^{TIR4})$ space as the one obtained with the whole OS radiance set, *i.e.*, our procedure for the optimization of the channel positions. Moreover, when comparing the RMSE values between calibration and validation cases, we observe small differences between RMSE maximum values (respectively minimum values), up to 0.09 K (respectively 0.01 K). These results, given the robustness of our validation method, justify the use of the calibration RMSE over the whole set of OS radiances as a procedure for optimizing the TRISHNA spectral configuration, notably in order to account for a large variability of input parameters.

V. Results and Recommended TRISHNA Configuration

A. Results of the optimization of channel positions

Figure 4 displays the RMSE values of SW calibration obtained for each spectral configuration corresponding to a pair of $(\lambda_c^{TIR3}, \lambda_c^{TIR4})$. The SW technique appears to be highly sensitive to the TIR3 and TIR4 positions with more than 3 K of difference between the maximum and minimum RMSEs values.

On the one hand, Figure 4 shows that for $\lambda_c^{TIR3} \leq 10.0$ μm, the calibration RMSE is larger than 3 K, and increases by more than 1.3 K alongside λ_c^{TIR4}, until the latter reaches 12.0 μm where the largest RMSEs are observed. The large RMSE

TABLE II
INSTRUMENTAL FEATURES FOR TRISHNA REFERENCE TIR3 AND TIR4 CHANNELS, INCLUDING CENTRAL WAVELENGTH λ_c, FULL WIDTH AT HALF MAXIMUM (FWHM), PARAMETERS a_i AND b_i FOR $Ne\Delta L_i$. ARE ALSO INDICATED THE RANGES OF VARIATION FOR TIR3 AND TIR4 CHANNEL POSITIONS, AS WELL AS THE RESULTING NUMBERS OF SPECTRAL CONFIGURATIONS AND OF SIMULATED RADIANCE MEASUREMENTS.

	TIR3	TIR4
λ_c^i (μm)	10.4	11.6
FWHM (μm)	0.7	1.0
a ($W^2.m^{-4}.sr^{-2}.\mu m^{-2}$,$\times 10^{-5}$)	4.47	4.32
b ($W.m^{-2}.sr^{-1}.\mu m^{-1}$,$\times 10^{-8}$)	8.13	175
λ_c^i variation (μm)	[9.5 μm ; 11 μm]	[10.5 μm ; 12 μm]
Number of ISRFs	241	
Number of L^{OS}	7,837,320	

values in this λ_c^{TIR3} interval are ascribed to the large spacing between TIR3 and TIR4 channels, the latter making invalid the main hypothesis of the SW method about near-equality of emissivities within SW channels. Similarly, increasing λ_c^{TIR4} when $\lambda_c^{TIR3} \leq 10.0$ μm also expands the space between TIR3 and TIR4, which induces larger differences between emissivities in the SW channels, and therefore larger values for RMSE on SW retrievals of land surface temperature. This result will be discussed in section VI.

On the other hand, for $\lambda_c^{TIR3} \geq 10.3$ μm, the RMSE tends to increase with the proximity of the two channels, *i.e.*, with decreasing λ_c^{TIR4}, and a local maximum occurs when both channels superimpose ($\lambda_c^{TIR3} = \lambda_c^{TIR4}$ axis, see bottom-right of Figure 4), with RMSE values around 3.5 K. This increase in RMSE values is ascribed to the decreasing difference in atmospheric transmittance between both SW channels. First, in the $\lambda_c^{TIR3} \geq 10.3$ μm region without ozone perturbation, TIR3 is systematically less affected by atmospheric perturbations than TIR4, since atmospheric disturbances related to water vapor increase with wavelength within the [9.5-12.5] μm spectral range (see Figure 6 in [87]). Second, the SW method performs better for large differences between atmospheric transmittance within both SW channels, provided that condition of near-equality of emissivities within SW channels is fulfilled. Overall, the optimal configuration is obtained for $\lambda_c^{TIR3} = 10.6$ μm and $\lambda_c^{TIR4} = 11.9$ μm with RMSE$_{cal}(T_{sur}^{SW})$ = 1.25 K, which is similar to the optimal configuration proposed in [42] for the same SW formulation. These results and their validity for other SW methods will be further discussed in section VI.

Figure 4 indicates an optimal region appears for $\lambda_c^{TIR3} \geq 10.4$ μm and $\lambda_c^{TIR4} \geq 11.3$ μm, with calibration RMSEs lower than 1.4 K, in accordance with the expected performance of the chosen SW formulation [51]. The reference spectral configuration (Table II) is located in this region, with a RMSE value of 1.39 K (red circle in Figure 4), which is satisfactory in terms of mission requirements (<1.5 K). However, considering a worst case scenario where the error margins on channel positions due to the instrument design could reach 0.2 μm (as given by the manufacturer, red rectangle in Figure 4), the RMSE could jump from 1.39 K to more than 2 K (see the cases where $\lambda_c^{TIR3} = 10.2$ μm). Hence, a more robust positioning of TIR3 and TIR4 should be found. Because of the complexity of the implementation of a detector with high cutoff frequency for TIR4, a conceptual issue exists against a shift of this channel toward higher wavelengths, which would lower the calibration RMSE. Thus, when considering TIR4 at its reference position of 11.6 μm, our results indicate an optimal position of TIR3 at 10.6 μm (purple circle in Figure 4). This new TIR3 position not only minimizes the SW RMSE value at 1.28 K, it also makes the spectral configuration more robust to uncertainties in both TIR3 and TIR4 positioning. Indeed, for a maximum channel misplacement of 0.2 μm, the largest RMSE value is lower than 1.44 K (purple rectangle in Figure 4), which is still within the expected performance of the chosen SW method.

TABLE III
TRISHNA RECOMMENDED TIR3 AND TIR4 CHANNELS CENTRAL WAVELENGTHS λ_c AND FWHMS WITH THEIR RESPECTIVE UNCERTAINTY. THE FWHM AND UNCERTAINTY VALUES ARE GIVEN BY THE INSTRUMENT MANUFACTURER.

	TIR3	TIR4
λ_c (μm)	10.6±0.15	11.6±0.15
FWHM (μm)	0.7±0.15	1.0±0.15

B. The recommended TRISHNA spectral configuration

As the aim of our study is to constrain the position of the TIR3 and TIR4 channels of the TRISHNA TIR instrument using sensitivity analyses of the SW method of [51] and a minimization process, we define a new set of positions for both spectral channels which is described in Table III and Figure 4 (purple circle). This new configuration is in agreement with the results of a similar study conducted with the TES algorithm in the context of the TRISHNA mission [77]. In this new configuration, the TIR3 channel is relocated at the optimal position of $\lambda_c^{TIR3} = 10.6$ μm. With this new configuration, a very light gain of 0.15 K is obtained on surface temperature RMSE as compared to the reference configuration. However, this configuration allows to relax the constraints to the manufacturer on the positioning of TIR3. Indeed, in case of large errors on channel positioning of 0.2 μm, the variation of RMSE is of at most 0.11 K with the new configuration, versus 0.75 K with the initial one.

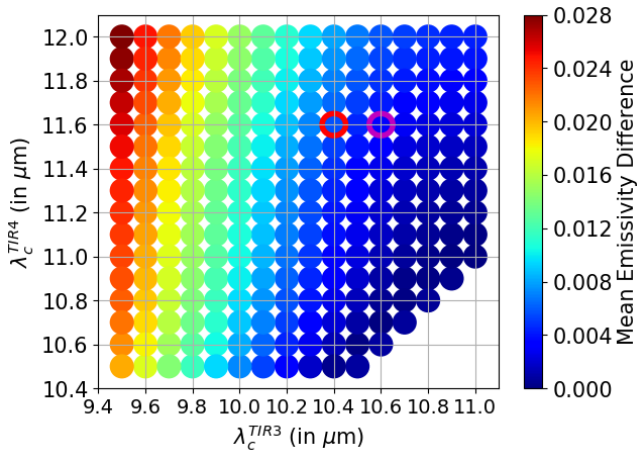

Fig. 5. Absolute average emissivity difference as observed between channels TIR3 and TIR4 for the 241 spectral configurations. The average emissivity spectrum is computed over the 271 spectra of the 'SAIL271' dataset. The red and purple circle respectively highlights the reference and recommended spectral configurations.

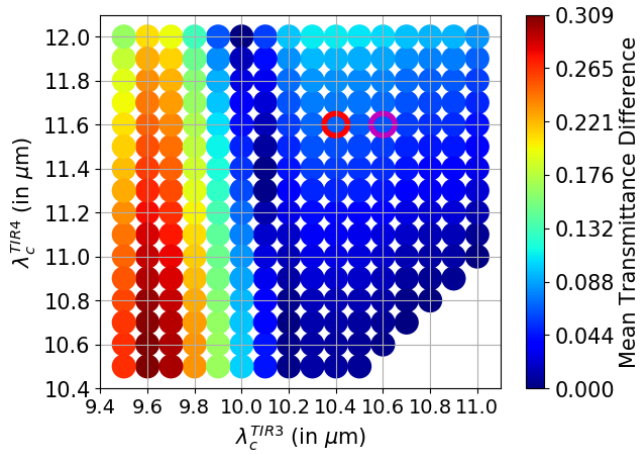

Fig. 6. Absolute average transmittance difference as observed between channels TIR3 and TIR4 for the 241 spectral configurations. The average transmittance spectrum is computed over the 24 profiles of the 'TIGR24' dataset. The red and purple circle respectively highlights the reference and recommended spectral configurations.

VI. Discussion

A. On the sensitivity to the difference in emissivity between TIR3 and TIR4

Figure 4 indicates an increase in RMSE values with decreasing λ_c^{TIR3} and increasing λ_c^{TIR4} in the $\lambda_c^{TIR3} \leq 10.0$ μm region. This trend is ascribed to increasing differences between the land surface emissivities captured by both SW channels. Figure 5 displays the absolute average emissivity difference between channels TIR3 and TIR4 for the 241 spectral configurations within the $(\lambda_c^{TIR3}, \lambda_c^{TIR4})$ space. These values are obtained by (1) computing the average emissivity spectrum over the 271 emissivity spectra of the 'SAIL271' dataset (see section III-B), (2) convolving this average emissivity spectrum with the 241 ISRFs to derive waveband emissivity within the TIR3 and TIR4 channels, and (3) calculating the absolute difference between average emissivity within the TIR3 and TIR4 channels.

Figure 5 shows a similar pattern as Figure 4 for the $\lambda_c^{TIR3} \leq 10.0$ μm region, with increasing differences in average emissivity as λ_c^{TIR3} decreases and λ_c^{TIR4} increases. This similitude supports the premise that the increasing RMSE along the bottom right to to top left axis in Figure 4 is mainly due to the increasing difference between surface emissivity within TIR3 and TIR4 channels. In order to further support this result, we compute the Spearman correlation coefficient between RMSE values displayed in Figure 4 and absolute average emissivity differences displayed in Figure 5. The obtained correlation coefficient is 0.737 with a very low p-value of 1.3×10^{-42}, which shows a significant correlation between both variables.

The sensitivity of the SW method performance to the difference in emissivity between SW channels raises the issue of correctly including this difference within the SW formulation. On the one hand, several SW formulations account for this difference, labeled $\Delta_{x,y}\epsilon$ in Equation 1 for the formulation we consider in the current study. On the other hand, the sensitivity we report here for this SW formulation performance to $\Delta_{x,y}\epsilon$ suggests that the corresponding term in Equation 1 is not appropriate. Therefore, further efforts have to be conducted on this issue, in order to develop a SW formulation that correctly accounts for $\Delta_{x,y}\epsilon$.

B. On the sensitivity to the difference in transmission between TIR3 and TIR4

Figure 4 also indicates a region of interest for TIR3 and TIR4 channels when $\lambda_c^{TIR3} \geq 10.3$ μm. For this region, average emissivity difference between TIR3 and TIR4 channels is lower than 0.01 (see Figure 5), which is in agreement with one of the underlying assumption of the SW method (i.e., low changes in surface emissivity between both channels). In this region, the SW method should perform very well when combining a channel with large atmospheric perturbations and another one with low atmospheric perturbations, so that difference between channel atmospheric transmittances is large. In order to verify the validity of this assumption, Figure 6 displays the absolute average transmittance difference between channels TIR3 and TIR4 for the 241 spectral configurations. These values are obtained with a method similar to that described in the previous section for the absolute average emissivity difference.

Comparison between Figure 6 and Figure 4 allows the following observations. First, there is no correlation between RMSE values displayed in Figure 4 and absolute average transmittance differences displayed in Figure 6, when dealing with the $\lambda_c^{TIR3} \leq 10.0$ μm region, while this region presents very high transmission differences between the two channels. This is ascribed to the fact that within this region, the SW assumption on low difference in surface emissivities between both channels is not verified. Second, an anti-correlation between RMSE values displayed in Figure 4 and absolute average transmittance differences displayed in Figure 6 is

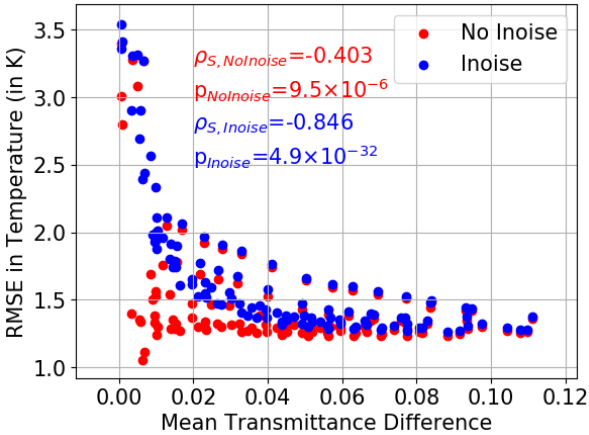

Fig. 7. RMSE values of the SW calibration as a function of the absolute average transmittance difference for the $\lambda_c^{TIR3} \geq 10.3$ μm region, without (red, 'No Inoise') and with (blue, 'Inoise') instrumental noise.

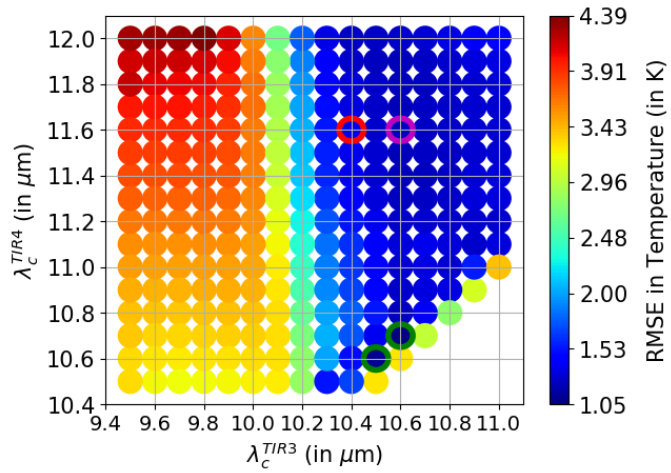

Fig. 8. RMSE values of the SW calibration for the 241 spectral configurations, without instrumental noise. The red and purple circle respectively highlights the reference and recommended spectral configurations. Both green circle highlights the minimum values of the calibration RMSE obtained, namely for $\lambda_c^{TIR3} = 10.5$ μm and $\lambda_c^{TIR4} = 10.6$ μ with a RMSE of 1.11 K, and for $\lambda_c^{TIR3} = 10.6$ μm and $\lambda_c^{TIR4} = 10.7$ μm with a RMSE of 1.06 K.

observed in the $\lambda_c^{TIR3} \geq 10.3$ μm region, with RMSE values on temperature decreasing with increasing transmittance differences, which is conform to the SW assumption on large difference between channel transmittances.

In order to further confirm this anti-correlation between the two set of variables, we display in Figure 7 the correlation, within the $\lambda_c^{TIR3} \geq 10.3$ μm region, between the RMSEs on SW surface temperature retrieval and the absolute average transmittance differences (blue points). The figure clearly shows the anti-correlation between both sets of variables, which is confirmed by a corresponding Spearman correlation coefficient of -0.846 and a very low p-value of 4.9×10^{-32}. This result highlights that when the observed emissivities in both SW channels are nearly equal, a channel configuration that maximize the transmittance difference has to be found for optimizing the channel positions.

C. On the sensitivity to the instrumental noise

As mentioned in the previous section, in the region of interest ($\lambda_c^{TIR3} \geq 10.3$ μm), the RMSE values on surface radiometric temperature increase with the relative proximity of the two SW channels (see Figure 4). Interestingly, we observe a different result when disregarding instrumental noise, as displayed in Figure 8. In that case, despite an overall variation of surface temperature RMSEs similar to the case with instrumental noise (see Figure 4 and red dots in Figure 7), the best configurations are found for ($\lambda_c^{TIR3} = 10.5$ μm, $\lambda_c^{TIR4} = 10.6$ μm) or ($\lambda_c^{TIR3} = 10.6$ μm, $\lambda_c^{TIR4} = 10.7$ μm), with respective RMSE values of 1.11 K and 1.06 K (see green circles in Figure 8).

This result is ascribed to small changes in emissivity and moderate changes in atmospheric transmittance around 10.6 μm. In the absence of instrumental noise, this induces that brightness temperatures measured in SW channels are different enough to correctly calibrate the SW coefficients. Thus, small variations of emissivity between channels allow the correct calibration of the SW coefficients, even for moderate change of transmittance. This suggests that difference in channel emissivity is the main driver for SW performance in our study case, as shown by the high Spearman correlation coefficient calculated in section VI-A. However, instrumental noise distorts variations of OS radiances between SW channels, where these radiances are originally driven by changes in surface emissivity and atmospheric transmittance. This makes the SW calibration less efficient, which explains the difference observed between Figure 4 and 8. Eventually, disregarding instrumental noise also degrades the Spearman correlation coefficient between RMSE values on SW retrievals and absolute average transmittance differences in the $\lambda_c^{TIR3} \geq 10.3$ μm region, with a coefficient of -0.403, although the global behavior is similar to that observed when considering instrumental noise (see Figure 7, red points versus blue points).

It should be noted that from a TRISHNA operational point of view, the TRISHNA TIR instrumental noise is mainly dependent on channel FWHM, which are considered fixed by mission requirements. However, Figure 8 only considers the variation of the SW performance according to physical underlying assumption, namely the difference in observed emissivity and atmospheric transmittance between TIR3 and TIR4 channels. Thus, this figure permits to verify the underlying physic principles of the SW method described in the previous sections.

D. On the applicability of our results to other SW formulations

The results reported in the current study theoretically depends on the formulation of the SW method to be chosen. However, since the overall variation of RMSEs observed in Figure 4 can be explained by SW hypothesis that are common to all existing formulations (see previous sections), it is valuable to explore if our results can be extended to other SW formulations. In that sense, we choose the Generalized Split Window (GSW) equation [49] which is routinely used for

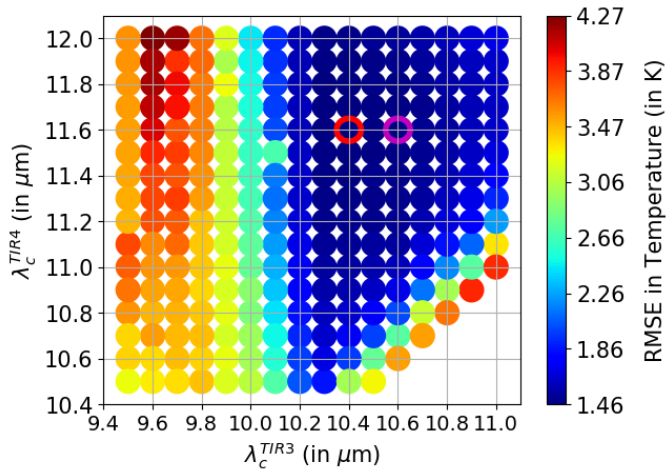

Fig. 9. RMSE values of the SW calibration for the 241 spectral configurations when using the formulation from [89] in place of that from [51] . The red and purple circle respectively highlights the reference and recommended spectral configurations.

MODIS (see for example [88]) or SEVIRI (see for example [89]). This formulation is different from the formulation of [51], since it does not explicitly account for AWVC and it is linear, but it still accounts for the difference in emissivity between the two channels. This SW formulation is calibrated using our set of OS radiances, and the obtained RMSEs are depicted in Figure 9.

It appears from Figure 9 that, despite some local differences, the overall trends obtained with this linear AWVC-independent SW formulation are very similar to those previously reported in Figure 4 with the non-linear AWVC-dependent SW formulation. First, the $\lambda_c^{TIR3} \geq 10.3$ μm region still corresponds to lower RMSE values, with a similar optimal position of TIR3 at $\lambda_c^{TIR3} = 10.6$ μm. Second, within this region of interest, the Spearman correlation coefficient also indicates an anti-correlation between RMSE values displayed in Figure 9 and absolute average transmittance differences displayed in Figure 6, with a value of -0.773 and a very low p-value of 1.22×10^{-23}. Third, a similar degradation of the SW method performance is observed in the $\lambda_c^{TIR3} \leq 10.0$ μm region, due to large differences between emissivities in TIR3 and TIR4 channels. Finally, when disregarding instrumental noise with the formulation of [89], we obtain similar results than those reported in the previous section, with a similar performance pattern in the $(\lambda_c^{TIR3}, \lambda_c^{TIR4})$ space and a minimum RMSE value obtained for the channel pair ($\lambda_c^{TIR3} = 10.6$ μm, $\lambda_c^{TIR4} = 10.7$). As mentioned in section VI-A for the SW formulation of [51], the observed sensitivity to the difference in emissivity between both SW channels highlights that this difference is not well considered into the SW formulation of [89], although is it explicitly included.

E. On the selection of atmospheric profiles

In section III-B, we highlighted the difference between the selected 'TIGR24' subset and the original TIGR dataset. Figure 3 shows that our selection of atmospheric profiles drastically reduces the density of dry atmosphere (AWVC < 2.5 g.cm^{-2}) as compared to the original dataset, with a 'TIGR24' subset that includes fewer dry atmospheres (11) than wet atmospheres (13). On the one hand, the current study is conducted in the context of the TRISHNA mission for which tropical regions such as India are of essential interest. On the other hand, AWVC is the main driver for atmospheric transmittance in the TIR domain. Therefore, it makes sense to optimize the TRISHNA SW channel positions by giving a large weight to the occurrence of wet atmospheres, and thus to account for a wide range of atmospheric transmittances. Subsequently, the 'TIGR24' subset is likely to enhance the dependency of the SW method to the difference between atmospheric transmittance within SW channels, and thus to increase the effect of atmospheric transmittance on the SW performance. Overall, studying the global SW performance requires to appropriately quantify the occurrence of dry and wet atmospheric profiles at the global extent. Such a quantification should be conducted in the context of the TRISHNA mission.

F. On the impacts of uncertainties on AWVC and land surface emissivity

Using SW formulation in Equation 1 induces that any SW retrieval of surface temperature is sensitive to uncertainty on AWVC, and to uncertainty on land surface emissivity within both SW channels. In order to evaluate the robustness of our bi-dimensional approach for SW channel location, we conduct a sensitivity study on land surface emissivity within the two SW channels, and on AWVC. We rely on [90] for uncertainty on AWVC retrievals from remotely sensed observations over the solar spectral domain. Thus, we set up RMSE and bias values to 0.2 g.cm^{-2} and 0.1 g.cm^{-2}, respectively. We rely on [46] for uncertainty on land surface emissivity retrievals from remotely sensed observations over the solar spectral domain. Thus, we set up the RMSE values to 0.02 for both TIR3 and TIR4 channels, and bias values to 0.01 and 0.015 for TIR3 and TIR4 channel, respectively. We consider two combinations for bias values on TIR3 and TIR4 channels: bias values equal to -0.01 and to +0.015, and bias values equal to +0.01 and to -0.015. In both AWVC and land surface emissivity cases, the RMSE values are included as an additional white noise within Equation 1.

Figure 10 displays the results related to uncertainty on SW channel emissivity, with bias values equal to -0.01 and to +0.015 on TIR3 and TIR4 channels, respectively. Beyond small differences in RMSE magnitude (< 0.3 K), we obtain very similar patterns within the (λ_c^{TIR3}, λ_c^{TIR4}) space, for all cases related to uncertainty on AWVC or on land surface emissivity (figures not shown). Most importantly, we obtain the same optimal location for TIR3 (given a fixed location of TIR4 at 11.6 μm) with or without uncertainty on SW channel emissivity and AWVC, *i.e.* λ_c^{TIR3} = 10.6. This result supports the conclusion that the SW channels location we obtained with our bi-dimensional approach is robust to these uncertainties.

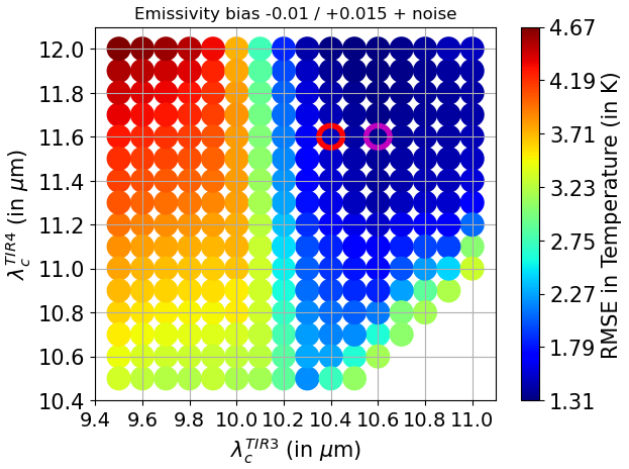

Fig. 10. RMSE values of the SW calibration with the 241 spectral configurations, when including uncertainty on SW channel emissivity (bias values equal to -0.01 and to +0.015 on TIR 3 and TIR 4 channels, respectively, and RMSE value equal to 0.02 for both channels). The red and purple circle respectively highlights the reference and recommended spectral configurations.

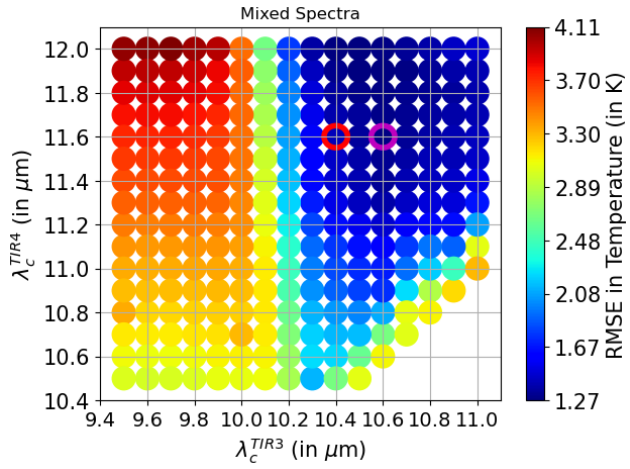

Fig. 11. RMSE values of the SW calibration with the 241 spectral configurations, by considering the linear mixing of the individual emissivity spectra considered in Case 1 (LAI = 0, bare soils) and in Case 2 (LAI$\geq$4, dense vegetation cover). Within the linear mixing, emissivity spectra for bare soil and dense vegetation cover have equal weights (50%-50%). The purple circle highlights the optimal spectral configuration corresponding to minimum RMSE values on SW retrievals.

G. On the inclusion of cavity effect within emissivity spectra

Evaluating the benefit of accounting for cavity effect requires to implement our bi-dimensional approach by using emissivity spectra without cavity effect. However, it is not possible to perform this implementation with all other variables being equal. Indeed, the SAIL-Thermique model is built to intrinsically account for cavity effects on the basis of soil reflectance and leave transmittance / reflectance, which prevents to reproduce the counterparts of the SAIL271 dataset without cavity effect. Therefore, we elaborate an alternative solution that consists in implementing our bi-dimensional sensitivity analysis while considering three cases where the cavity effect is not included into the land surface emissivity spectra of the SAIL271 database.

- Case 1: we consider the spectra of the SAIL271 dataset that correspond to LAI = 0, and thus to bare soils.
- Case 2: we consider the spectra of the SAIL271 dataset that correspond to LAI = 7, and thus to dense vegetation canopies with low cavity effect.
- Case 3: we consider the linear mixing of the individual emissivity spectra considered in Case 1 (bare soils) and in Case 2 (dense vegetation canopies). Within the linear mixing, emissivity spectra for bare soil and dense vegetation canopies have equal weights (50%-50%), in order to simulate an intermediate situation between bare soil and dense vegetation canopies.

Figure 11 displays the results obtained for Case 3 (i.e., linear mixing of individual spectra). We obtain very similar results for both bare soil and dense vegetation canopies (figures not shown), since the patterns of RMSE on SW retrievals within the (λ_c^{TIR3}, λ_c^{TIR4}) space are very similar across the three cases. Beyond small differences in RMSE magnitude, the most important result is that we obtain the same optimal locations for TIR3 (given a fixed location of TIR4 at 11.6 μm) when including (Figure 4) or not (Figure 11) the cavity effect, *i.e.* λ_c^{TIR3} = 10.6 μm. Furthermore, we do not report significant difference in our proposition for SW channels location as compared to former studies that do not account for cavity effect (e.g., [42]). Both results discussed in this section support the conclusion that accounting for cavity effects when using the SW method is not a critical issue, as opposed to the use of TES method [38].

VII. Conclusion

In the context of the TRISHNA mission, we propose an original approach for optimizing the sensor spectral configuration in accordance to the related performance of the SW method. We conduct a sensitivity analysis of the SW method to the channel positions along with a minimization process. The approach is original for two reasons. First, it relies on a simulated dataset of land surface emissivity spectra that accounts for radiance trapping within vegetation canopy, namely the cavity effect (i.e., emissivity increase). Second, it relies on a bi-dimensional approach where both SW channels can slide within respective intervals. This permits to identify extreme values for the SW method performance within the spectral space defined by the sliding channels, but especially permits to define a spectral configuration that is robust to uncertainties on channel positions.

From the operational viewpoint of the TRISHNA mission, the current study provides a new TIR spectral configuration as compared to the manufacturer baseline, notably with TIR3 channel located at λ_c^{TIR3} = 10.6 μm, to be combined with TIR4 channel located at λ_c^{TIR4} = 11.6 μm. This new configuration permits to slightly reduce the error on surface temperature retrievals as compared to the reference configuration (0.15 K), but significantly reduces this error when accounting for uncertainties on channel location (0.6 K).

From a scientific viewpoint, our study reveals a high sensitivity of the SW method to the TIR3 and TIR4 SW channel

positions, where the error on surface radiometric temperature can go up to 3 K within the spectral space defined by the sliding channels. Furthermore, the bi-dimensional approach permits to highlight that the observed sensitivity is due to the underlying physical principles of the SW method, notably by revealing two distinct regions for the SW method performance in the $(\lambda_c^{TIR3}, \lambda_c^{TIR4})$ space:

1) the $\lambda_c^{TIR3} \leq 10.0$ μm region, where the underlying hypothesis about near-equality of channel emissivities is not valid, and where the performance therefore decreases with increasing distance between TIR3 and TIR4;
2) the $\lambda_c^{TIR3} \geq 10.3$ μm region, where the differences in channel emissivities are small enough to make valid the underlying hypothesis about near-equality, and where the SW method performance is mainly driven by the differences in channel transmittance.

The clear observation of these two regions shows that the two underlying hypothesis of the SW method (i.e., near-equality for land surface emissivities and large difference between atmospheric transmittances within the SW channels) are not verified in a same region of the $(\lambda_c^{TIR3}, \lambda_c^{TIR4})$ space. This explains that performances of the SW method reported in the literature is more or less satisfactory [30], [51], [55].

When disregarding instrumental noise, optimal configurations correspond to high proximity of TIR3 and TIR4 channels, namely ($\lambda_c^{TIR3} = 10.5$ μm, $\lambda_c^{TIR4} = 10.6$), and ($\lambda_c^{TIR3} = 10.6$ μm, $\lambda_c^{TIR4} = 10.7$). In that case, the SW method can be successfully calibrated with small differences in atmospheric transmittance between both channels, provided that the differences between surface emissivity in both channels are very low. This result, combined with the high Spearman correlation coefficient of 0.737 obtained between the surface temperature RMSEs and average emissivity differences dataset, supports the idea that the difference between surface emissivities in the two SW channels is the main driver for the SW method performance. This high sensitivity to the difference between land surface emissivity within both SW channels also shows that current SW formulations do not adequately consider this difference, since they donot efficiently correct the related effects on surface temperature retrievals. This highlights the need for further efforts on new SW formulations.

By applying our study on two structurally different SW formulations, we revealed similar behaviors of the SW performance. This strengthens the hypothesis that the sensitivity of the SW formulation proposed by [51] to differences in surface emissivity and transmittance between SW channels, which are the underlying physical assumptions of the SW method, can be generalized to several SW formulations. Besides, we do not report significant differences in SW channel locations as compared to former studies that do not account for cavity effect, or as compared to the use in the current study of emissivity spectra without cavity effect. This underlines that calibrating any SW formulation over a dataset of emissivity spectra with cavity effect is likely not to be a critical issue, conversely to the results reported by [38] for the TES method.

For future studies, our results notably highlight the importance of considering the validity space of the SW method when optimizing the spectral channel positions. Furthermore, the SW method performance is sensitive to the difference in atmospheric transmittance between SW channels, which hints that locating the upper channel above 12 μm may improve the performance. Further investigations on the matter should be conducted for the design of future TIR missions. Additionally, it is necessary to conduct further sensitivity analysis of existing SW formulations to the difference between land surface emissivity in both SW channels, in order to better account for this parameter. Finally, the SW performance is sensitive to instrumental noise, which highlights the importance of investigating sensor technologies that reduce instrumental noise for future TIR missions, the goal being to obtain spectral configurations with very close SW channels.

Acknowledgment

This work was funded by the French Space Agency (CNES, contract 181154) in the context of the preparation of the TRISHNA mission.

References

[1] G. C. Hulley and S. J. Hook, "Generating consistent land surface temperature and emissivity products between aster and modis data for earth science research," *IEEE Transactions on Geoscience and Remote Sensing*, vol. 49, no. 4, pp. 1304–1315, 2010.

[2] K. Ogawa, T. Schmugge, F. Jacob, and A. French, "Estimation of broadband land surface emissivity from multi-spectral thermal infrared remote sensing," *Agronomie*, vol. 22, no. 6, pp. 695–696, 2002.

[3] ——, "Estimation of land surface window (8–12 μm) emissivity from multi-spectral thermal infrared remote sensing—a case study in a part of sahara desert," *Geophysical Research Letters*, vol. 30, no. 2, 2003.

[4] M. Mira, A. Olioso, B. Gallego-Elvira, D. Courault, S. Garrigues, O. Marloie, O. Hagolle, P. Guillevic, and G. Boulet, "Uncertainty assessment of surface net radiation derived from landsat images," *Remote sensing of Environment*, vol. 175, pp. 251–270, 2016.

[5] G. Yan, Z.-H. Jiao, T. Wang, and X. Mu, "Modeling surface longwave radiation over high-relief terrain," *Remote Sensing of Environment*, vol. 237, p. 111556, 2020.

[6] G. Bigeard, B. Coudert, J. Chirouze, S. Er-Raki, G. Boulet, E. Ceschia, and L. Jarlan, "Ability of a soil-vegetation-atmosphere transfer model and a two-source energy balance model to predict evapotranspiration for several crops and climate conditions," *Hydrology and Earth System Sciences*, vol. 23, no. 12, pp. 5033–5058, 2019.

[7] T. N. Carlson and G. P. Petropoulos, "A new method for estimating of evapotranspiration and surface soil moisture from optical and thermal infrared measurements: the simplified triangle," *International Journal of Remote Sensing*, vol. 40, no. 20, pp. 7716–7729, 2019.

[8] D. Courault, F. Jacob, V. Benoit, M. Weiss, O. Marloie, J.-F. Hanocq, E. Fillol, A. Olioso, G. Dedieu, P. Gouaux *et al.*, "Influence of agricultural practices on micrometerological spatial variations at local and regional scales," *International Journal of Remote Sensing*, vol. 30, no. 5, pp. 1183–1205, 2009.

[9] A. N. French, F. Jacob, M. C. Anderson, W. P. Kustas, W. Timmermans, A. Gieske, Z. Su, H. Su, M. F. McCabe, F. Li *et al.*, "Surface energy fluxes with the advanced spaceborne thermal emission and reflection radiometer (aster) at the iowa 2002 smacex site (usa)," *Remote sensing of environment*, vol. 99, no. 1-2, pp. 55–65, 2005.

[10] M. Galleguillos, F. Jacob, L. Prévot, A. French, and P. Lagacherie, "Comparison of two temperature differencing methods to estimate daily evapotranspiration over a mediterranean vineyard watershed from aster data," *Remote Sensing of Environment*, vol. 115, no. 6, pp. 1326–1340, 2011.

[11] M. Galleguillos, F. Jacob, L. Prévot, P. Lagacherie, and S. Liang, "Mapping daily evapotranspiration over a mediterranean vineyard watershed," *IEEE Geoscience and Remote Sensing Letters*, vol. 8, no. 1, pp. 168–172, 2010.

[12] M. Gómez, A. Olioso, J. Sobrino, and F. Jacob, "Retrieval of evapotranspiration over the alpilles/reseda experimental site using airborne polder sensor and a thermal camera," *Remote Sensing of Environment*, vol. 96, no. 3-4, pp. 399–408, 2005.

[13] F. Jacob, A. Olioso, X. F. Gu, Z. Su, and B. Seguin, "Mapping surface fluxes using airborne visible, near infrared, thermal infrared remote sensing data and a spatialized surface energy balance model," *Agronomie*, vol. 22, no. 6, pp. 669–680, 2002.

[14] C. Montes, J.-P. Lhomme, J. Demarty, L. Prévot, and F. Jacob, "A three-source svat modeling of evaporation: Application to the seasonal dynamics of a grassed vineyard," *Agricultural and forest meteorology*, vol. 191, pp. 64–80, 2014.

[15] C. Montes and F. Jacob, "Comparing landsat-7 etm+ and aster imageries to estimate daily evapotranspiration within a mediterranean vineyard watershed," *IEEE Geoscience and Remote Sensing Letters*, vol. 14, no. 3, pp. 459–463, 2017.

[16] N. Pardo, M. L. Sánchez, J. Timmermans, Z. Su, I. A. Pérez, and M. A. García, "Sebs validation in a spanish rotating crop," *Agricultural and forest meteorology*, vol. 195, pp. 132–142, 2014.

[17] R. K. Vinukollu, E. F. Wood, C. R. Ferguson, and J. B. Fisher, "Global estimates of evapotranspiration for climate studies using multi-sensor remote sensing data: Evaluation of three process-based approaches," *Remote Sensing of Environment*, vol. 115, no. 3, pp. 801–823, 2011.

[18] B. Bayat, C. van der Tol, and W. Verhoef, "Integrating satellite optical and thermal infrared observations for improving daily ecosystem functioning estimations during a drought episode," *Remote Sensing of Environment*, vol. 209, pp. 375–394, 2018.

[19] Y. Inoue, A. Olioso, and W. Choi, "Dynamic change of co2 flux over bare soil field and its relationship with remotely sensed surface temperature," *International Journal of Remote Sensing*, vol. 25, no. 10, pp. 1881–1892, 2004.

[20] A. Olioso, Y. Inoue, S. Ortega-Farias, J. Demarty, J.-P. Wigneron, I. Braud, F. Jacob, P. Lecharpentier, C. Ottlé, J.-C. Calvet *et al.*, "Future directions for advanced evapotranspiration modeling: Assimilation of remote sensing data into crop simulation models and svat models," *Irrigation and Drainage Systems*, vol. 19, no. 3-4, pp. 377–412, 2005.

[21] M. Weiss, F. Jacob, and G. Duveiller, "Remote sensing for agricultural applications: A meta-review," *Remote Sensing of Environment*, vol. 236, p. 111402, 2020.

[22] G. Hulley, S. Hook, J. Fisher, and C. Lee, "Ecostress, a nasa earth-ventures instrument for studying links between the water cycle and plant health over the diurnal cycle," in *2017 IEEE International Geoscience and Remote Sensing Symposium (IGARSS)*. IEEE, 2017, pp. 5494–5496.

[23] J. B. Fisher, B. Lee, A. J. Purdy, G. H. Halverson, M. B. Dohlen, K. Cawse-Nicholson, A. Wang, R. G. Anderson, B. Aragon, M. A. Arain *et al.*, "Ecostress: Nasa's next generation mission to measure evapotranspiration from the international space station," *Water Resources Research*, vol. 56, no. 4, p. e2019WR026058, 2020.

[24] B. Koetz, W. Bastiaanssen, M. Berger, P. Defourney, U. Del Bello, M. Drusch, M. Drinkwater, R. Duca, V. Fernandez, D. Ghent *et al.*, "High spatio-temporal resolution land surface temperature mission-a copernicus candidate mission in support of agricultural monitoring," in *2016 IEEE International Geoscience and Remote Sensing Symposium (IGARSS)*. IEEE, 2018, pp. 8160–8162.

[25] J.-P. Lagouarde, B. Bhattacharya, P. Crébassol, P. Gamet, S. Babu, G. Boulet, X. Briottet, K. M. Buddhiraju, S. Cherchali, I. Dadou *et al.*, "The indian-french trishna mission: Earth observation in the thermal infrared with high spatio-temporal resolution," in *IGARSS 2018-2018 IEEE International Geoscience and Remote Sensing Symposium*. IEEE, 2018, pp. 4078–4081.

[26] J.-P. Lagouarde, B. Bhattacharya, P. Crébassol, P. Gamet, D. Adlakha, C. Murthy, S. Singh, M. Mishra, R. Nigam, P. Raju *et al.*, "Indo-french high-resolution thermal infrared space mission for earth natural resources assessment and monitoring-concept and definition of trishna," in *ISPRS-GEOGLAM-ISRS Joint International Workshop on "Earth Observations for Agricultural Monitoring"*, vol. 42, 2019, p. 403.

[27] F. Jacob, T. Vidal, A. Lesaignoux, A. Olioso, M. Weiss, F. Nerry, S. Jacquemoud, P. Gamet, K. Caillault, L. Labarre, A. French, T. Schmugge, X. Briottet, and J. P. Lagouarde, "A simulation-based error budget of the tes method for the design of the spectral configuration of the micro-bolometer based mistigri thermal infrared sensor," *IEEE Transactions on Geoscience and Remote Sensing*, vol. in revision, no. -, pp. –, 2021.

[28] P. Dash, F.-M. Göttsche, F.-S. Olesen, and H. Fischer, "Land surface temperature and emissivity estimation from passive sensor data: Theory and practice-current trends," *International Journal of Remote Sensing*, vol. 23, no. 13, pp. 2563–2594, 2002.

[29] F. Jacob, T. Schmugge, A. Olioso, A. French, D. Courault, K. Ogawa, F. Petitcolin, G. Chehbouni, A. Pinheiro, and J. Privette, "Modeling and inversion in thermal infrared remote sensing over vegetated land surfaces," in *Advances in Land Remote Sensing*. Springer, 2008, pp. 245–291.

[30] Z.-L. Li, B.-H. Tang, H. Wu, H. Ren, G. Yan, Z. Wan, I. F. Trigo, and J. A. Sobrino, "Satellite-derived land surface temperature: Current status and perspectives," *Remote Sensing of Environment*, vol. 131, pp. 14–37, 2013.

[31] A. French, T. Schmugge, J. Ritchie, A. Hsu, F. Jacob, and K. Ogawa, "Detecting land cover change at the jornada experimental range, new mexico with aster emissivities," *Remote Sensing of Environment*, vol. 112, no. 4, pp. 1730–1748, 2008.

[32] A. Gillespie, S. Rokugawa, T. Matsunaga, J. S. Cothern, S. Hook, and A. B. Kahle, "A temperature and emissivity separation algorithm for advanced spaceborne thermal emission and reflection radiometer (aster) images," *IEEE Transactions on Geoscience and Remote Sensing*, vol. 36, no. 4, pp. 1113–1126, 1998.

[33] A. R. Gillespie, S. Rokugawa, S. J. Hook, T. Matsunaga, and A. B. Kahle, "Temperature/emissivity separation algorithm theoretical basis document, version 2.4," *ATBD contract NAS5-31372, NASA*, 1999.

[34] A. R. Gillespie, E. A. Abbott, L. Gilson, G. Hulley, J.-C. Jiménez-Muñoz, and J. A. Sobrino, "Residual errors in aster temperature and emissivity standard products ast08 and ast05," *Remote Sensing of Environment*, vol. 115, no. 12, pp. 3681–3694, 2011.

[35] W. T. Gustafson, A. R. Gillespie, and G. J. Yamada, "Revisions to the aster temperature/emissivity separation algorithm," in *2nd International Symposium on Recent Advances in Quantitative Remote Sensing*. Global Change Unit, University of Valencia Torrent, Spain, 2006.

[36] G. Hulley, S. Hook, and A. Baldridge, "Aster land surface emissivity database of california and nevada," *Geophysical Research Letters*, vol. 35, no. 13, 2008.

[37] F. Jacob, F. Petitcolin, T. Schmugge, E. Vermote, A. French, and K. Ogawa, "Comparison of land surface emissivity and radiometric temperature derived from modis and aster sensors," *Remote Sensing of Environment*, vol. 90, no. 2, pp. 137–152, 2004.

[38] F. Jacob, A. Lesaignoux, A. Olioso, M. Weiss, K. Caillault, S. Jacquemoud, F. Nerry, A. French, T. Schmugge, X. Briottet *et al.*, "Reassessment of the temperature-emissivity separation from multispectral thermal infrared data: Introducing the impact of vegetation canopy by simulating the cavity effect with the sail-thermique model," *Remote Sensing of Environment*, vol. 198, pp. 160–172, 2017.

[39] T. Schmugge, S. Hook, and C. Coll, "Recovering surface temperature and emissivity from thermal infrared multispectral data," *Remote Sensing of Environment*, vol. 65, no. 2, pp. 121–131, 1998.

[40] T. Schmugge, A. French, J. C. Ritchie, A. Rango, and H. Pelgrum, "Temperature and emissivity separation from multispectral thermal infrared observations," *Remote Sensing of Environment*, vol. 79, no. 2-3, pp. 189–198, 2002.

[41] J. A. Sobrino, J. C. Jiménez-Muñoz, L. Balick, A. R. Gillespie, D. A. Sabol, and W. T. Gustafson, "Accuracy of aster level-2 thermal-infrared standard products of an agricultural area in spain," *Remote Sensing of Environment*, vol. 106, no. 2, pp. 146–153, 2007.

[42] J. A. Sobrino and J. C. Jiménez-Muñoz, "Minimum configuration of thermal infrared bands for land surface temperature and emissivity estimation in the context of potential future missions," *Remote sensing of environment*, vol. 148, pp. 158–167, 2014.

[43] X. Zheng, Z.-L. Li, F. Nerry, and X. Zhang, "A new thermal infrared channel configuration for accurate land surface temperature retrieval from satellite data," *Remote Sensing of Environment*, vol. 231, p. 111216, 2019.

[44] E. Neinavaz, A. K. Skidmore, and R. Darvishzadeh, "Effects of prediction accuracy of the proportion of vegetation cover on land surface emissivity and temperature using the ndvi threshold method," *International Journal of Applied Earth Observation and Geoinformation*, vol. 85, p. 101984, 2020.

[45] Q. Vanhellemont, "Combined land surface emissivity and temperature estimation from landsat 8 oli and tirs," *ISPRS Journal of Photogrammetry and Remote Sensing*, vol. 166, pp. 390–402, 2020.

[46] J. C. Jiménez-Muñoz, J. A. Sobrino, A. Gillespie, D. Sabol, and W. T. Gustafson, "Improved land surface emissivities over agricultural areas using aster ndvi," *Remote Sensing of Environment*, vol. 103, no. 4, pp. 474–487, 2006.

[47] J. A. Sobrino, J. C. Jimenez-Munoz, and L. Paolini, "Land surface temperature retrieval from landsat tm 5," *Remote Sensing of environment*, vol. 90, no. 4, pp. 434–440, 2004.

[48] A. Vidal, "Atmospheric and emissivity correction of land surface temperature measured from satellite using ground measurements or satellite data," *Remote Sensing*, vol. 12, no. 12, pp. 2449–2460, 1991.

[49] Z. Wan and J. Dozier, "A generalized split-window algorithm for retrieving land-surface temperature from space," *IEEE Transactions on Geoscience and Remote Sensing*, vol. 34, no. 4, pp. 892–905, 1996.

[50] A. Olioso, "Simulating the relationship between thermal emissivity and the normalized difference vegetation index," *International Journal of Remote Sensing*, vol. 16, no. 16, pp. 3211–3216, 1995.

[51] J. Sobrino and N. Raissouni, "Toward remote sensing methods for land cover dynamic monitoring: Application to morocco," *International Journal of Remote Sensing*, vol. 21, no. 2, pp. 353–366, 2000.

[52] J. Sobrino, J. El Kharraz, and Z.-L. Li, "Surface temperature and water vapour retrieval from modis data," *International Journal of Remote Sensing*, vol. 24, no. 24, pp. 5161–5182, 2003.

[53] H. Liu, S. Tang, J. Hu, S. Zhang, and X. Deng, "An improved physical split-window algorithm for precipitable water vapor retrieval exploiting the water vapor channel observations," *Remote Sensing of Environment*, vol. 194, pp. 366–378, 2017.

[54] L. M. McMillin, "Estimation of sea surface temperatures from two infrared window measurements with different absorption," *Journal of Geophysical Research*, vol. 80, no. 36, pp. 5113–5117, 1975.

[55] F. Becker and Z.-L. Li, "Towards a local split window method over land surfaces," *Remote Sensing*, vol. 11, no. 3, pp. 369–393, 1990.

[56] C. Coll and V. Caselles, "A split-window algorithm for land surface temperature from advanced very high resolution radiometer data: validation and algorithm comparison," *Journal of Geophysical Research: Atmospheres*, vol. 102, no. D14, pp. 16 697–16 713, 1997.

[57] J. Sobrino, Z. Li, M. Stoll, and F. Becker, "Multi-channel and multi-angle algorithms for estimating sea and land surface temperature with atsr data," *International Journal of Remote Sensing*, vol. 17, no. 11, pp. 2089–2114, 1996.

[58] F. Becker and Z.-L. Li, "Surface temperature and emissivity at various scales: Definition, measurement and related problems," *Remote Sensing Reviews*, vol. 12, no. 3-4, pp. 225–253, 1995.

[59] J. Sobrino and M. Romaguera, "Land surface temperature retrieval from msg1-seviri data," *Remote Sensing of Environment*, vol. 92, no. 2, pp. 247–254, 2004.

[60] Y. A. Anton and Y. K. Ross, "Emissivity of a soil vegetation system," *Soviet Journal of Remote Sensing*, vol. 7, no. 5, pp. 859–869, 1990.

[61] L. Chen, Z.-L. Li, Q. Liu, S. Chen, Y. Tang, and B. Zhong, "Definition of component effective emissivity for heterogeneous and non-isothermal surfaces and its approximate calculation," *International Journal of Remote Sensing*, vol. 25, no. 1, pp. 231–244, 2004.

[62] C. Francois, C. Ottle, and L. Prevot, "Analytical parameterization of canopy directional emissivity and directional radiance in the thermal infrared. application on the retrieval of soil and foliage temperatures using two directional measurements," *International Journal of Remote Sensing*, vol. 18, no. 12, pp. 2587–2621, 1997.

[63] P. Guillevic, J. Gastellu-Etchegorry, J. Demarty, and L. Prévot, "Thermal infrared radiative transfer within three-dimensional vegetation covers," *Journal of Geophysical Research: Atmospheres*, vol. 108, no. D8, 2003.

[64] O. Merlin and A. Chehbouni, "Different approaches in estimating heat flux using dual angle observations of radiative surface temperature," *International Journal of Remote Sensing*, vol. 25, no. 1, pp. 275–289, 2004.

[65] A. Olioso, G. Sòria, J. Sobrino, and B. Duchemin, "Evidence of low land surface thermal infrared emissivity in the presence of dry vegetation," *IEEE Geoscience and Remote Sensing Letters*, vol. 4, no. 1, pp. 112–116, 2007.

[66] L. Pérez-Planells, E. Valor, R. Niclòs, C. Coll, J. Puchades, and M. Campos-Taberner, "Evaluation of six directional canopy emissivity models in the thermal infrared using emissivity measurements," *Remote Sensing*, vol. 11, no. 24, p. 3011, 2019.

[67] B. Cao, M. Guo, W. Fan, X. Xu, J. Peng, H. Ren, Y. Du, H. Li, Z. Bian, T. Hu *et al.*, "A new directional canopy emissivity model based on spectral invariants," *IEEE Transactions on Geoscience and Remote Sensing*, vol. 56, no. 12, pp. 6911–6926, 2018.

[68] B. Cao, Q. Liu, Y. Du, J.-L. Roujean, J.-P. Gastellu-Etchegorry, I. F. Trigo, W. Zhan, Y. Yu, J. Cheng, F. Jacob *et al.*, "A review of earth surface thermal radiation directionality observing and modeling: Historical development, current status and perspectives," *Remote Sensing of Environment*, vol. 232, p. 111304, 2019.

[69] V. Caselles, E. Rubio, C. Coll, and E. Valor, "Thermal band selection for the prism instrument: 3. optimal band configurations," *Journal of Geophysical Research: Atmospheres*, vol. 103, no. D14, pp. 17 057–17 067, 1998.

[70] P. Deschamps and T. Phulpin, "Atmospheric correction of infrared measurements of sea surface temperature using channels at 3.7, 11 and 12 μm," *Boundary-Layer Meteorology*, vol. 18, no. 2, pp. 131–143, 1980.

[71] D. Sun and R. T. Pinker, "Estimation of land surface temperature from a geostationary operational environmental satellite (goes-8)," *Journal of Geophysical Research: Atmospheres*, vol. 108, no. D11, 2003.

[72] X. Ye, H. Ren, R. Liu, Q. Qin, Y. Liu, and J. Dong, "Land surface temperature estimate from chinese gaofen-5 satellite data using split-window algorithm," *IEEE Transactions on Geoscience and Remote Sensing*, vol. 55, no. 10, pp. 5877–5888, 2017.

[73] J. Sobrino, J. El Kharraz, and Z.-L. Li, "Surface temperature and water vapour retrieval from modis data," *International Journal of Remote Sensing*, vol. 24, no. 24, pp. 5161–5182, 2003.

[74] Y. Julien, J. A. Sobrino, and W. Verhoef, "Changes in land surface temperatures and ndvi values over europe between 1982 and 1999," *Remote Sensing of Environment*, vol. 103, no. 1, pp. 43–55, 2006.

[75] M. Vesperini, F.-M. Breon, and D. Tanre, "Atmospheric water vapor content from spaceborne polder measurements," *IEEE transactions on geoscience and remote sensing*, vol. 37, no. 3, pp. 1613–1619, 1999.

[76] A. Makarau, R. Richter, D. Schläpfer, and P. Reinartz, "Apda water vapor retrieval validation for sentinel-2 imagery," *IEEE Geoscience and Remote Sensing Letters*, vol. 14, no. 2, pp. 227–231, 2016.

[77] T. H. G. Vidal, P. Gamet, A. Olioso, and F. Jacob, "A sensitivity study of the TES algorithm to TIR channels positioning : constraints on the TRISHNA TIR instrument," *Remote Sensing of Environment*, p. Submitted, 2021.

[78] L. Poutier, C. Miesch, X. Lenot, V. Achard, and Y. Boucher, "Comanche and cochise: two reciprocal atmospheric codes for hyperspectral remote sensing," in *2002 AVIRIS Earth Science and Applications Workshop Proceedings*, 2002, pp. 1059–0889.

[79] A. Berk and G. P. Anderson, "Impact of modtran® 5.1 on atmospheric compensation," in *2008 IEEE International Geoscience and Remote Sensing Symposium (IGARSS)*, vol. 3. IEEE, 2008, pp. III–127.

[80] G. Girouard, A. Bannari, A. El Harti, and A. Desrochers, "Validated spectral angle mapper algorithm for geological mapping: comparative study between quickbird and landsat-tm," in *XXth ISPRS congress, geo-imagery bridging continents, Istanbul, Turkey*, 2004, pp. 12–23.

[81] A. Olioso, F. Jacob, and M. Weiss, "First evaluation of land surface emissivity spectra simulated with the sail-thermique model," in *2018 IEEE International Geoscience and Remote Sensing Symposium (IGARSS)*. IEEE, 2018, pp. 3951–3954.

[82] P. Guillevic, J. Gastellu-Etchegorry, J. Demarty, and L. Prévot, "Thermal infrared radiative transfer within three-dimensional vegetation covers," *Journal of Geophysical Research: Atmospheres*, vol. 108, no. D8, 2003.

[83] H. Ren, R. Liu, G. Yan, Z.-L. Li, Q. Qin, Q. Liu, and F. Nerry, "Performance evaluation of four directional emissivity analytical models with thermal sail model and airborne images," *Optics express*, vol. 23, no. 7, pp. A346–A360, 2015.

[84] F. Chevallier, A. Chédin, F. Chéruy, and J.-J. Morcrette, "Tigr-like atmospheric-profile databases for accurate radiative-flux computation," *Quarterly Journal of the Royal Meteorological Society*, vol. 126, no. 563, pp. 777–785, 2000.

[85] F. Jacob, X. Gu, J.-F. Hanocq, N. Tallet, and F. Baret, "Atmospheric corrections of single broadband channel and multidirectional airborne thermal infrared data: application to the reseda experiment," *International Journal of Remote Sensing*, vol. 24, no. 16, pp. 3269–3290, 2003.

[86] T. Hastie, R. Tibshirani, and J. Friedman, *The elements of statistical learning: data mining, inference, and prediction*. Springer Science & Business Media, 2009.

[87] J.-P. Lagouarde, M. Bach, J. A. Sobrino, G. Boulet, X. Briottet, S. Cherchali, B. Coudert, I. Dadou, G. Dedieu, P. Gamet *et al.*, "The mistigri thermal infrared project: scientific objectives and mission specifications," *International Journal of Remote Sensing*, vol. 34, no. 9-10, pp. 3437–3466, 2013.

[88] P. C. Guillevic, J. C. Biard, G. C. Hulley, J. L. Privette, S. J. Hook, A. Olioso, F. M. Göttsche, R. Radocinski, M. O. Román, Y. Yu *et al.*, "Validation of land surface temperature products derived from the visible infrared imaging radiometer suite (viirs) using ground-based and heritage satellite measurements," *Remote Sensing of Environment*, vol. 154, pp. 19–37, 2014.

[89] I. F. Trigo, I. T. Monteiro, F. Olesen, and E. Kabsch, "An assessment of remotely sensed land surface temperature," *Journal of Geophysical Research: Atmospheres*, vol. 113, no. D17, 2008.

[90] O. Hagolle, M. Huc, C. Desjardins, S. Auer, and R. Richter, "Maja atbd algorithm theoretical basis document - technical report. 2017," tech. rep., CNES+ CESBIO and DLR, Tech. Rep., 2017. [Online]. Available: https://www.theia-land.fr/wp-content-theia/uploads/sites/2/2018/12/atbd_maja_071217.pdf (05 June 2021)